# Enhanced Charge-Transfer Kinetics by Anion Surface Modification of LiFePO$_4$

Kyu-Sung Park,[†,‡] Penghao Xiao,[§] So-Yeon Kim,[‡] Anthony Dylla,[§] Young-Min Choi,[‡] Graeme Henkelman,[§] Keith J. Stevenson,[§] and John B. Goodenough*,[†]

[†]Texas Materials Institute, University of Texas at Austin, Austin, Texas 78712, United States
[‡]Battery group, Samsung Advanced Institute of Technology (SAIT), PO Box 111, Suwon 440-600, South Korea
[§]Department of Chemistry and Biochemistry, University of Texas at Austin, Austin, Texas 78712, United States

S Supporting Information

ABSTRACT: Despite the great achievement in understanding the materials properties and powder engineering of LiFePO$_4$, the chemical bonding at the surface has been almost ignored. Herein, we demonstrate that the undercoordinated Fe^{2+}/Fe^{3+} redox couple at the surface gives a high barrier for charge transfer, but it can be stabilized by nitrogen or sulfur adsorption. The surface modification improves greatly the charge transfer kinetics and the charge/discharge performance of a LiFePO$_4$ cathode. Density functional theory (DFT) calculation estimates the origin of the improvement in terms of an electronic and ionic contribution based on a surface model probed by time of flight secondary ion mass spectrometry (TOF-SIMS); the calculation agrees well with an experimental rate-constant analysis.

KEYWORDS: Li-ion battery, insertion compounds, interface chemistry
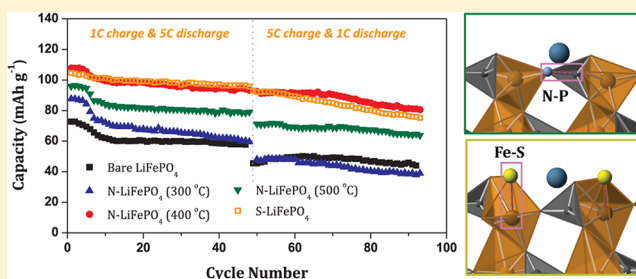
INTRODUCTION

To reduce the effects of fossil fuels on global warming and air pollution, alternative energy sources at an affordable price are urgently needed. The intermittency of wind and solar energy makes mandatory large-scale energy storage as a complement to these alternative energy sources, and rechargeable batteries can provide both portable and stationary storage of the electrical energy generated from wind and radiant solar power. Moreover, rechargeable batteries that power electric vehicles offer not only a distributed energy store, which can make the cost of battery storage more acceptable, but also a relief from distributed sources of air pollution. LiFePO$_4$ offers a cathode alternative for a Li-ion battery (LIB) that contains low-cost, environmentally benign materials, is safe, and has a competitive energy density with a proven long cycle life at high rates of charge/discharge. These features make it a worthy target for further reduction of its reversible capacity loss at the highest charge/discharge rates desired for powering an electric vehicle.

A LiFePO$_4$ cathode has a theoretical capacity of 170 mAh g^{-1} and operates at a voltage of V = 3.45 V versus lithium, which is safely above the HOMO of the organic liquid-carbonate electrolyte. Moreover, the strong covalent bonding within the (PO$_4$)$^{3-}$ anion keeps the top of the O-2p bands well below the active redox energy, which prevents oxygen evolution at full charge even at high temperatures.[1−4] Although a two-phase reaction between LiFePO$_4$ and FePO$_4$ creates a poor electronic conductivity, which lowers the electrochemical capacity at higher charge/discharge rates, carbon coating of nanosized LiFePO$_4$ particles has largely solved this problem.[5−7] Although Li$^+$ diffusion is confined to one-dimensional (1-D) channels along the b-axis,[8−10] the nanosized LiFePO$_4$ particles crystallize in the form of platelets with the b-axis perpendicular to the plates, which facilitates Li access to all the particle volume. With proper quality control, high-rate LiFePO$_4$ cathodes have been successfully introduced into practical LIBs of very long life. Nevertheless, there is some reversible capacity loss at high rates owing to the resistance of Li$^+$ transport across the electrolyte/electrode interface. We report here a reduction of this charge-transfer resistance by the introduction of nitrogen or sulfur to the surface of the LiFePO$_4$ particles. We have also undertaken a theoretical study of how the barrier to direct Li$^+$ transport between the electrolyte and the b-axis channels is modified by the substitution of nitrogen or sulfur for surface oxygen on the (010) surface plane of the LiFePO$_4$ platelets.

RESULTS AND DISCUSSION

Experimental Results. Uncoated LiFePO$_4$ particles were used to provide clean surfaces for adsorption/chemisorption of N or S. Highly uniform LiFePO$_4$ powders synthesized hydrothermally by microwave heating were heat-treated further at 600 °C in a reducing atmosphere to ensure the well-ordered surface and bulk structure needed for good electrochemical

properties.[11,12] After the heat-treatment, the bare $LiFePO_4$ particles were single-phased with lattice parameters $a = 10.321(1)$, $b = 6.0021(5)$, and $c = 4.6904(5)$ nm; and the particle size varied from 100 to 500 nm owing to particle sintering at 600 °C (see the Supporting Information for materials characterization, Figures S1−S5). To introduce nitrogen to the surface, the bare $LiFePO_4$ particles were postannealed under a NH_3 atmosphere at various temperatures from 300 to 500 °C. To introduce sulfur, bare $LiFePO_4$ powder was exposed to sulfur vapor at 400 °C and subsequently annealed at 400 °C in a pure vacuum to remove elemental sulfur from the surface. The surfaces of bare $LiFePO_4$ and $FePO_4$ particles were modified by NH_3 gas and S vapor, and these surface-modified samples are denoted N-$LiFePO_4$, N-$FePO_4$, and S-$LiFePO_4$, S-$FePO_4$, respectively.

The particle size and the morphology were little changed by the postannealing treatments, regardless of the annealing temperatures; changes in the lattice parameters are also less than 0.05% compared to the reference values. Three Raman bands observed above 400 cm^{-1} for both the bare and N-$LiFePO_4$ samples are due to intramolecular $(PO_4)^{3-}$ symmetric (951 cm^{-1}) and asymmetric (996 and 1068 cm^{-1}) stretching vibrations (Figure S5, Supporting Information). Raman bands located in the 100−400 cm^{-1} region are typically assigned to translatory intermolecular modes involving lattice vibrations of $(PO_4)^{3-}$ units and Fe^{2+} ions.[13] These modes are often weak and difficult to assign correctly. The lack of peaks in the 1200−1700 cm^{-1} region related to the broad D and G modes of graphite indicate that there was no carbon coating of the particle surface or heterogeneously mixed with the $LiFePO_4$ crystallites. Previous studies have observed a broadening of the intramolecular symmetric stretching mode of $(PO_4)^{3-}$ in $LiFePO_4$ that can be attributed to a lower degree of order in the lattice owing to doping of other transition metals.[13] While aliovalent doping was not used in this study, significant diffusion of nitrogen or sulfur into the bulk of $LiFePO_4$ may similarly be expected to distort the crystal structure. No broadening was observed in the intramolecular $(PO_4)^{3-}$ mode at 951 cm^{-1} for the N-$LiFePO_4$ compared to the reference material. This result, along with X-ray diffraction (XRD), shows that the bulk of the N-$LiFePO_4$ remains unchanged. The Raman spectrum of S-$LiFePO_4$ also shows bands normally associated with $LiFePO_4$, which suggests that the $LiFePO_4$ structure is preserved upon sulfur exposure. Several bands not associated with $LiFePO_4$ are also present. The bands at 320, 339, and 374 cm^{-1} are likely associated with surface-bound Fe−S species.[14]

Time of flight secondary ion mass spectrometry (TOF-SIMS) was used to interrogate the surface layer of N- and S-$LiFePO_4$ to confirm the presence of N and S elements and to determine the relative depth of their distribution. Figure 1a shows depth profiles for various temperature treatments of N-$LiFePO_4$ along with the reference material. A major ionic species had P−N bonds; surface adsorbed NH_3^+ and NH_4^+ ions gave a significantly smaller signal intensity. Theoretical calculation also supports the N-replacement of O in the $(PO_4)^{3-}$ unit; therefore, ion fragments containing subspecies of that polyatomic ion should be an accurate marker for detection of surface nitrogen. Finally, the sum of PN^+ and PNH_2^+ were selected as the surface nitridation ions to construct the depth profiles. The two-dimensional (2-D) profile for the bare $LiFePO_4$ shows that there is a small amount of N-species, but the concentration is significantly lower near the surface compared to NH_3-treated $LiFePO_4$ samples. For the N-
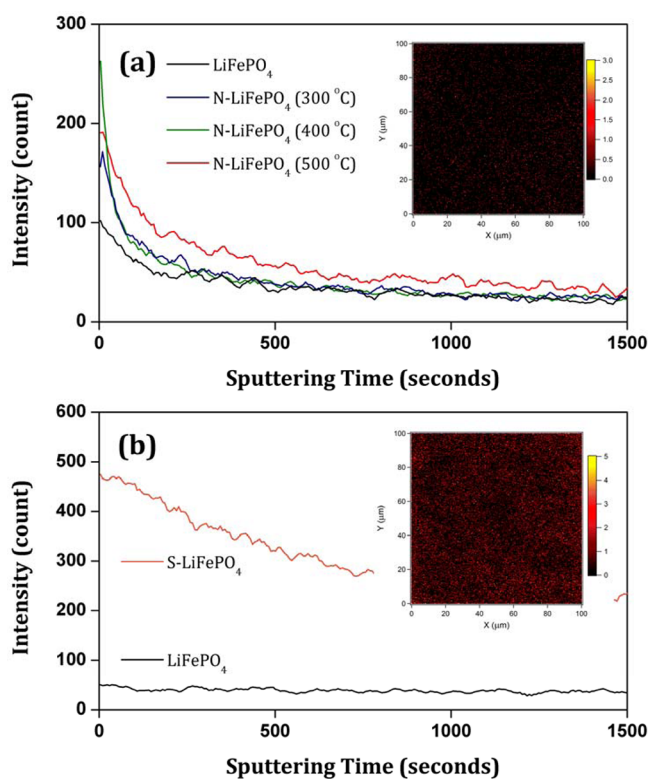

Figure 1. TOF-SIMS depth profiles, with Bi_3^{2+} sputtering, of (a) the sum of PN^+ and PNH_2^+ ion species for N-$LiFePO_4$ and (b) the sum of FeS^+ and $FeSH^+$ ion fragments for S-$LiFePO_4$. Inset images in a and b show areal distributions of the PN^+/PNH_2^+ ions for N-$LiFePO_4$ prepared at 400 °C and the $FeS^+/FeSH^+$ ions for S-$LiFePO_4$, respectively.

$LiFePO_4$ prepared at 300 °C, the initial concentration is lower than both the 400 and 500 °C samples but above that of the bare $LiFePO_4$, indicating surface nitridation. The N-$LiFePO_4$ prepared at 400 °C has the highest relative concentration of N-species at the surface while the signal sharply drops to a baseline level at deeper depths suggesting that the N-species are confined to the surface. Finally, the N-$LiFePO_4$ prepared at 500 °C exhibits the second-highest relative N-species concentration at the surface, but the signal profile is significantly more diffuse throughout the depth profiling experiment. This observation indicates that degradation of the material at the surface and near surface is occurring owing to the higher reaction temperature, which leads to further diffusion of nitrogen into the particle,[15] as is also clearly shown in the high-resolution TEM images (Figure S4, Supporting Information).

Figure 1b shows similar depth profiles comparing the bare $LiFePO_4$ to the S-$LiFePO_4$. In this case, the major ion species have Fe−S bonds, and theoretical calculation also confirms that sulfur atoms prefer to bond at dangling surface Fe sites. The presence of elemental sulfur can be excluded because it brings a high-voltage decomposition. After annealing under sulfur vapor, the material shows an electrochemical decomposition at around 4.45 V vs Li^+/Li, but this feature disappears after a following anneal under pure vacuum. Therefore, we investigated FeS^+ and $FeSH^+$ ion fragments as indicators of surface sulfur interactions. In contrast to the N-$LiFePO_4$, the concentration profile of S-$LiFePO_4$ in the surface layer is more diffuse and of higher relative concentration compared to the bare $LiFePO_4$. This

observation suggests that sulfur reacts differently at the LiFePO$_4$ surface than nitrogen and is consistent with the theoretical lowest-energy surface calculations showing Fe−S bonding as opposed to P−N bonding. Knock-in effects by the bombardment of the surface with Bi$_3^{2+}$ clusters may also explain the more diffuse nature of the 2-D profile for S-LiFePO$_4$. Since the FeS-related species are heavier, it is likely that a higher proportion of those species relative to the lighter PN-related species will be pushed into the surface rather than ejected into the mass analyzer; therefore, a more broad relative concentration profile would be observed. Results from the TOF-SIMS analysis show that both nitrogen and sulfur bond at the surface of LiFePO$_4$, but do not diffuse significantly into the bulk of the crystal. Though we cannot quantify the sputtering depth, we are confident that we are only interrogating the surface layers based on the low dose of Bi$_3^{2+}$ sputtering used in dynamic-mode operation.

Electrochemical properties of the surface-modified LiFePO$_4$ have been characterized by the discharge-rate capability and high-rate cycling tests at room temperature shown in Figure 2
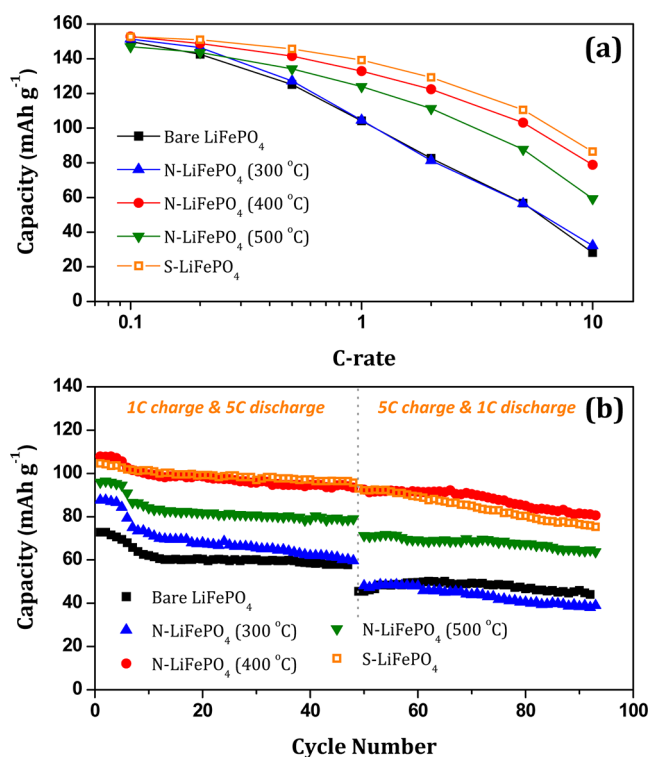

Figure 2. (a) Discharge rate capability of the bare and N-/S-LiFePO$_4$ half-cells evaluated after C/10 charging to 4.5 V vs Li$^+$/Li in each cycle. (b) Discharge capacities at the asymmetric charge/discharge cycling conditions. The first 50 cycles were tested at 1C charge/5C discharge in 2.5−4.5 V range, and after that, the current densities were reversed.

(see also Supporting Information, Figure S6). The bare LiFePO$_4$ discharge specific capacity is 149.9 mAh g^{-1} at a C/10 rate, it falls to 28.2 mAh g^{-1} at 10C. However, after introducing N onto the surface at 400 °C, the capacity at 10C is significantly increased to 78.9 mAh g^{-1}, while the 300 °C annealing shows negligible difference in the rate capability. Considering the higher amount of nitrogen on the particle surface after the 400 °C annealing, the data suggests that nitrogen can significantly influence the interfacial charge-

transfer kinetics. After 500 °C annealing, however, the capacity is lowered to 147 mAh g^{-1} at C/10, but it still has a better rate performance than that of the bare LiFePO$_4$. The initial capacity decrease is consistent with the high-resolution TEM and TOF-SIMS data that showed a surface decomposition at 500 °C owing to a highly reducing condition, but the presence of nitrogen still has a positive effect on the discharge kinetics. For the sulfur-introduced LiFePO$_4$, the capacity at C/10 is 152.6 mAh g^{-1}, and at higher current densities, it shows better rate capability than that of N-LiFePO$_4$. At the 10C rate, the capacity of S-LiFePO$_4$ is 86.4 mAh g^{-1}. Sulfur on the surface has brought a strong positive effect on the rate performance that is comparable to that of the N-LiFePO$_4$ prepared at 400 °C.

Asymmetric charge/discharge cycling also gives an interesting result (Figure 2b). 1C charge followed by a 5C discharge confirms the great difference in the high-rate capacities between bare and N-/S-LiFePO$_4$ half-cells. The capacity trend in the first cycling condition is similar to that of the rate performance result: S-LiFePO$_4$ and N-LiFePO$_4$ prepared at 400 °C show average capacities of 99.1 and 97.9 mAh g^{-1}, respectively; the bare LiFePO$_4$ has 61.4 mAh g^{-1}. After changing the charge/discharge current densities in the reverse condition (5C charge and the following 1C discharge), the discharge capacity generally drops in every case, which should be due to less charging capacity at the higher current, 5C. From the result, it is clear that N-/S-LiFePO$_4$ cells have less capacity drop; strikingly, the drop almost disappeared in the case of S-LiFePO$_4$ and N-LiFePO$_4$ prepared at 400 °C. The surface modification by N and S atoms enhances significantly not only the discharge rate-performance but also the charging kinetics.

Theoretical Results. Since calculation has indicated a high activation energy for Li$^+$ surface diffusion,[16] we have studied how the barrier to direct Li$^+$ transport between the electrolyte and the *b*-axis channels can be modified by nitrogen or sulfur surface species. In such a study, it is important to identify the characteristics of the surface (010) plane. The strong covalent bonding of the (PO$_4$)$^{3-}$ anion makes it reasonable to assume that it is the Li and/or Fe sites that become undercoordinated at the surface as recently calculated for a relaxed surface (010) plane.[17] However, an exposure to NH$_3$, P−N bonds may form as a result of loss of oxygen from the (PO$_4$)$^{3-}$ groups. Undercoordination of the Fe changes the Fe^{3+}/Fe^{2+} redox energy both at and a little below the (010) surface, and these changes can be modified by chemisorption of different anion species on the surface. Among the anions that can replace surface oxygen or (PO$_4$)$^{3-}$ anions, nitrogen and sulfur (respective electronic configuration: [He]2s^{2}2p^3 and [Ne]-3s^{2}3p^4) are particularly interesting because each atom has a different ionic size, formal charge, and electronegativity.

To correlate the presence of N and S atoms on the specific surface sites and the improved electrochemical properties, density functional theory (DFT) calculations of the surface-modified FePO$_4$ have been performed. TOF-SIMS results show that N and S appear only on the surface of LiFePO$_4$; nitrogen is found mainly with phosphorus as P−N, while sulfur is found with iron as Fe−S. Using these results as guidance, we replaced an O atom closest to a *b*-channel with a nitrogen atom in a PO$_4$ group in the N-LiFePO$_4$ case; in the S-LiFePO$_4$ case, we put a sulfur atom on top of a surface Fe site, forming a Fe−S bond. These binding sites were found to be energetically favorable.

Figure 3 shows the calculated binding energy of a single Li$^+$ ion as it diffuses from the (010) surface of FePO$_4$ along the *b*-channel. In the bare FePO$_4$, Li$^+$ binds weakly on the surface and
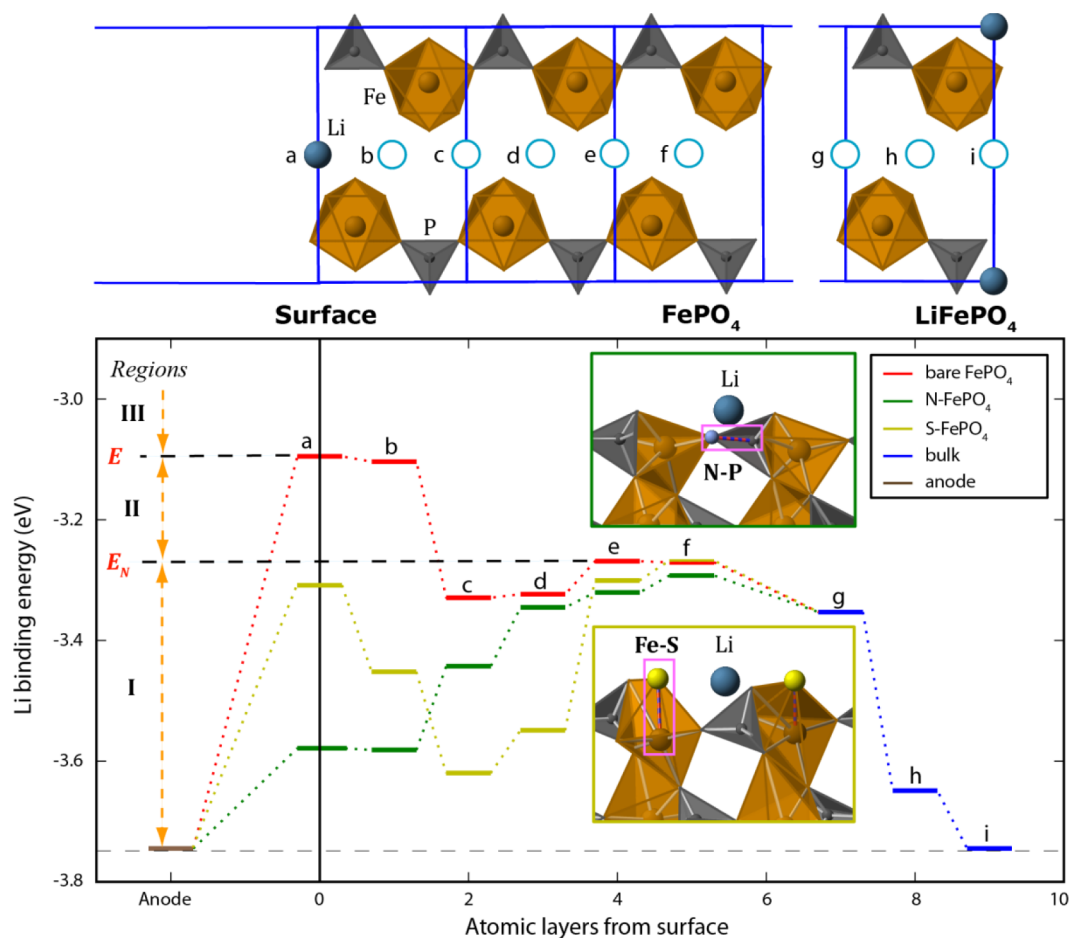
Figure 3. Energy landscapes of Li moving from the surface into the b-channel of bare $FePO_4$ and in the presence of N and S. Inset crystallographic images represent the structural modification forming N−P and Fe−S bonds after introducing N and S atoms on the surface.

subsurface sites (a- and b-sites, respectively) owing to a low coordination of Li and Fe on the surface and a structural distortion of the subsurface site. Where Li^+ reaches an $FePO_4$ bulk site, the binding is stronger by 0.18 eV. Li binds most strongly in the $LiFePO_4$ phase. In the $FePO_4$ phase, there is a Coulomb attraction between Li^+ and its electron, which is located on a neighboring Fe^{2+} center. In the $LiFePO_4$ phase, several Li^+ can share the same Fe^{2+} center making the Coulomb energy correspondingly lower. The binding energies for the three regions (surface, $FePO_4$, and $LiFePO_4$) are −3.10, −3.28, and −3.75 eV, respectively, consistent with values reported in the literature.[16,17]

Since the barriers for Li hopping between sites are relatively small (0.2−0.3 eV) and do not vary significantly between phases,[16,18] the binding energies along the b-channel can serve as the minimum energy path (MEP) for Li diffusion into and out of the material. As shown in Figure 3, the weak binding of Li to the surface site determines the overall barrier for both lithiation and delithiation. Theoretically, if the voltage is below 3.75 V during lithiation, Li should be able to intercalate into the cathode and form the $LiFePO_4$ phase. In practice, however, the rate at this voltage is too low to be measured. There are two reasons for this observation: first, diffusion of Li^+ into the material has to overcome a relatively high barrier (3.75 − 3.10 = 0.65 eV), and second, those intercalating Li^+ must agglomerate to nucleate the $LiFePO_4$ phase. Only when the voltage approaches 3.28 V does the discharge current become

measurable because at this voltage, isolated Li^+ ions are stable in the $FePO_4$ phase. Both N- and S-modification decrease the total barrier by strengthening the Li^+ binding on surface sites, thus improving the rate performance. After the surface modification, the barrier is determined by the Li^+ binding energy in the $FePO_4$ bulk phase.

Focusing on the lithiation (discharge) processes, we can compare the rate of the bare and N-/S-$FePO_4$ to see whether experimental discharging rates match what we expect from the calculated energy landscape (Figure 3). If the anode energy level increases (by decreasing the applied voltage between anode and cathode), the overall lithiation barrier height will change. If the anode energy level is below that of the weakest binding site, the intercalation barrier is the energy difference between these two sites. If the anode energy level is above the weakest binding site energy, there is no additional barrier above the diffusion barrier between sites, and so, the intercalation rate is limited by diffusion (or other mass transport factors in the experimental apparatus).

We take the diffusion barrier in this high-energy anode regime to be the barrier for Li^+ transport from the anode to the surface site, denoted ΔE_N for the N-$FePO_4$ and ΔE for the bare $FePO_4$. ΔE_N and ΔE are independent of the applied voltage. Next, we denote the binding energy of Li^+ in a bulk site of N-$FePO_4$ as E_N, and the surface site binding energy of the bare $FePO_4$ as E. E_N and E are the binding energies of Li at the highest energy (weakest binding) sites for the N-$FePO_4$ and the

bare FePO$_4$, respectively. The relative rate constants for the bare and N-FePO$_4$ cases follow eq 1. Here, we assume the same prefactor A for all the lithiation processes and use V' as a converted value of the applied voltage in eV scale ($V' = -V$ in value).

(I) $V' < E_N$: $\dfrac{k}{k_N} = \dfrac{A\ e^{-\beta(E-V')}}{A\ e^{-\beta(E_N-V')}} = e^{-\beta(E-E_N)}$

(II) $E_N < V' < E$:
$$\frac{k}{k_N} = \frac{A\ e^{-\beta(E-V')}}{A\ e^{-\beta(\Delta E_N)}} = e^{-\beta(E-\Delta E_N-V')}$$

(III) $V' > E$: $\dfrac{k}{k_N} = \dfrac{A\ e^{-\beta(\Delta E)}}{A\ e^{-\beta(\Delta E_N)}} = e^{-\beta(\Delta E-\Delta E_N)}$ (1)

As shown in eq 1, if $V' < E_N$ and $V' > E$ (regions I and III), the ratio of rate constants is constant, while in between the ratio increases as the voltage decreases (V' increases). In the first region, $V' < E_N$, the current is too small to be measured in experiment, as discussed; in the third region, $V' > E$, the voltage is too high and the system is far from equilibrium, which may complicate the discussion. So we will compare with the experiment the rate constant trend for $E_N < V < E$ in region II.

These same arguments hold for the dependence of rate on the applied voltage in the S-FePO$_4$.

A potential step chronocoulometry was performed to evaluate the calculated energy barriers according to eq 1(II) (see Supporting Information, Figure S7). To estimate the rate constant, k, from the experimental data, we assumed the lithiation process to be a simple first-order reaction. Because lithium-ion diffusion into the cathode is equivalent to vacancies moving out, the rate equation is written in terms of vacancy concentration C_V. The backward reaction can be ignored when the discharge time, t, is small.

$$\frac{dC_V(t)}{dt} = -kC_V(t) \qquad (2)$$

$$C_V(t) = C_V(0)\ e^{-kt} \qquad (3)$$

Converting C_V to the capacity, Q.

$$Q(\infty) - Q(t) = Q(\infty)\ e^{-kt} \qquad (4)$$

$$\ln\left(1 - \frac{Q(t)}{Q(\infty)}\right) = -kt \qquad (5)$$

$\ln(1 - Q(t)/Q(\infty))$ vs time curves of the bare and N-/S-FePO$_4$ are found to be linear in the short-time domain as shown in Figure S7 (Supporting Information).[19] In this short-time domain, the discharge reaction is interfacial charge-transfer controlled, not diffusion-controlled. From the curve, the ratio of the rate constants of the bare and N-/S-FePO$_4$ are plotted in Figure 4 to show the voltage-dependent variation as predicted from eq 1. The experimental trend clearly confirms the calculation. In both N- and S-FePO$_4$ cells, as the applied voltage decreases, the k/k_N and k/k_S ratio increases. At around 3.2 and 3.1 V, it reaches a plateau, where the ratio stops increasing as the voltage decreases (a transition between region II and III, where the lithium binding energy $E = -3.10$ eV). Since sulfur has a higher surface coverage than N, as shown in Figure 1, the slope of k/k_S may be higher than k/k_N of N-FePO$_4$. Moreover,
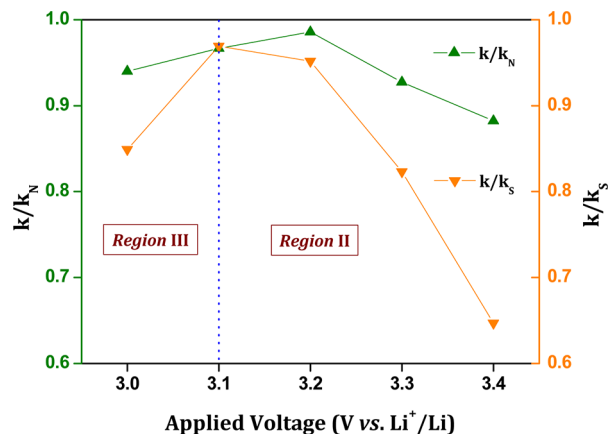

Figure 4. Ratio of the rate constants between the bare and N-/S-LiFePO$_4$. The rate equation is estimated in terms of filling up vacant Li-sites in FePO$_4$ during constant-voltage discharge by the equation $\ln(1 - Q(t)/Q(\infty)) = -kt$.

regardless of the voltage values, the rate constants of N-/S-FePO$_4$ are always higher than that of the bare FePO$_4$, which must enhance the high-rate performance of the electrochemical cell.

In this section, we discuss changes to the Li binding due to surface doping. The Li binding energy has two primary contributions: the electronic part (e$^-$) and the ionic part (Li$^+$). For the bare FePO$_4$, weak binding at the surface is primarily due to the electronic contribution. In the bulk, the Fe d$_z^2$ orbital extends over two neighboring oxygen atoms; on the surface, Fe is undercoordinated, and its d$_z^2$ orbital extends over only one oxygen neighbor. The surface Fe–O bond is, therefore, stronger, and the energy of the corresponding antibonding state (populated by the extra electron from Li) is higher. In the b-site of Figure 3, the ionic part is responsible for weak binding. Li$^+$ in the site is fully coordinated, but the cage space where Li$^+$ can sit is bigger than in a bulk site. The distance between Li$^+$ and half of the surrounding O^{2-} is increased, raising the Coulombic energy. In the a-site of Figure 3, Li$^+$ is missing an attractive interaction from an O^{2-} center; it is also missing a repulsion interaction from an Fe^{3+} center. As a result of these two competing effects (which are comparable in magnitude), the ionic contribution of Li$^+$ binding to an a-site is comparable to a bulk FePO$_4$ site.

N-substitution can stabilize Li$^+$ in both a- and b-sites because it affects the binding energies in both the electronic part and the ionic part. First, as shown in Figure S8 (Supporting Information), nitrogen provides an empty 2p state in the band gap, so that the extra electron coming with Li$^+$ does not have to go to the higher energy Fe 3d states. Nitrogen lowers the HOMO energy after Li intercalation. Second, nitrogen is more negatively charged than oxygen and has a stronger Coulomb interaction with Li$^+$. Comparison of the atomic structures of a-, b-, and c-sites are shown in Figure S10 (Supporting Information). As can be seen, Li$^+$ in the b-site is displaced toward the nitrogen, as compared to the b-site in the bare material, showing the attractive interaction.

An analysis of the S-doped surface shows that the mechanism for increasing Li$^+$ binding is different from that of nitrogen. Sulfur binds directly to a surface Fe atom, providing full coordination of the Fe center. The electronic environment of Li$^+$ is similar to that in the bulk and the binding energy is close to that of Li in bulk FePO$_4$. The binding of Li$^+$ in the b- and c-

subsurface sites increases with respect to the surface a-site. The reason is not due to the electronic structure. A comparison of the density of states (DOS) is shown in Figure S9 (Supporting Information). These data show that S raises the HOMO energy level after Li^+ intercalation, indicating that the electron binding energy is weaker. The stronger Li^+ binding is therefore due to ionic interactions. Sulfur induces a dramatic geometric distortion to the surface. The PO_4 surface groups are rotated, and the subsurface Fe centers are noncoplanar (see red box in Figure S10, Supporting Information). This change in geometry gives rise to the strong Li^+ binding found in the b-, c-, and d-sites.

CONCLUSION

In summary, we have shown that the presence of nitrogen or sulfur on the surface of $LiFePO_4$ can greatly improve the surface electrochemistry during charge/discharge. The surface bonding state characterized with TOF-SIMS indicates that nitrogen preferably substitutes for oxygen in the $(PO_4)^{3-}$ anions and sulfur dominantly bonds to the undercoordinated Fe site. DFT calculations show that the total barrier for Li transfer is decreased by strong Li binding on surface sites in the presence of N or S. The theoretical result is backed by comparison of rate constants during potential-step chronocoulometry. For N-$LiFePO_4$, nitrogen can provide a more stable 2p state than surface Fe 3d state for electron transfer and also has a stronger Coulomb interaction with Li^+ owing to the more negative charge. For S-$LiFePO_4$, sulfur mainly stabilizes the surface Fe 3d antibonding states. Modification of a surface can tune the surface energy levels and change the total barrier for the charge transfer kinetics.

EXPERIMENTAL SECTION

Synthesis and Post-treatment. Powder Li_3PO_4 (Aldrich) was added to a 200 mL aqueous solution of $FeSO_4 \cdot 7H_2O$ (Aldrich) with a molar ratio of 1:1 (0.25 mol L^{-1}) at room temperature. The mixture was thoroughly agitated with a paint shaker for 1 h. The obtained homogeneous suspension was transferred into microwave hydrothermal synthesis system (MARS 230/60, CEM Corp.). The system was operated at a frequency of 2.45 GHz and a power of 1600 W with continuous stirring to ensure a homogeneous reaction. The sample temperature was ramped to 230 °C and kept at 230 °C for 15 min under the hydrothermal condition. After the reaction, the reactor was cooled to room temperature by a built-in cooling fan in the system. The precipitated product was filtered off, washed several times with distilled water, and finally dried. The as-synthesized powder was heat-treated at 600 °C for 4 h under 5% H_2 in Ar atmosphere.

For ammonia-exposed $LiFePO_4$ preparation, the crystalline $LiFePO_4$ powder was postannealed under an NH_3 flow of 100 sccm for 30 min. The annealing temperature was set to 300, 400, and 500 °C. Ultrapure Ar atmosphere with 300 sccm was kept during purging and ramping. For sulfur-exposed $LiFePO_4$ preparation, the synthesized $LiFePO_4$ powder was placed into sulfur vapor at 400 °C for 20 min. The sulfur atmosphere was made by thermal evaporation of sulfur powder (99.999% pure, Alfa Aesar) in a vacuum-sealed quartz tube; to remove elemental sulfur from the powder, static vacuum annealing at 400 °C without sulfur vapor followed.

Characterization. Powder X-ray diffraction data were obtained with a Philips X'Pert Pro MPD diffractometer (40 kV, 40 mA; Cu Kα radiation). The data acquisition time was set to 10 s on each 0.02° step, and the 2θ value ranged from 15° to 90° in the θ-2θ mode. The high-resolution XRD patterns were refined with X'Pert Highscore software. Powder morphology and the surface structure were examined with SEM (Hitachi S4700) and TEM (TECNAI G^2 F20 S-TWIN, FEI). Raman data was taken in a Renishaw In Via microscope system utilizing a 514.5 nm Argon laser in back scattering configuration. The

beam was focused with a 50× aperture, resulting in an approximately 2-μm-diameter sampling cross section. The instrument was calibrated to the Stokes Raman signal at 521 cm^{-1} in a bulk single crystal of Si with the [110] lattice oriented normal to the laser. To avoid sample damage by the laser, three accumulations at low power (10%, 3 mW) with 10 s exposure time were used.

Time-of-flight secondary-ion mass spectroscopy (TOF-SIMS) was performed on a TOF-SIMS 5 by ION-TOF GMBH with Bi_3^{2+} ions accelerated at 3 kV in dynamic mode. In this mode of operation, a single ion source is used as both the analysis (primary) gun and the sputtering (secondary) gun in order to interrogate gently the surface layer. A randomly rastered 150 mm^2 analysis area (256 × 256 pixel resolution) was used to acquire the 3-D ion distribution maps. Secondary ions were detected in positive-ion mode, and an electron flood gun was introduced during analysis to avoid charging of the surface. Pelletized samples were loaded and allowed to purge for a minimum of 12 h before introduction to the main analysis chamber. All analyses were performed with the main analysis chamber pressures between 5 and 9×10^{-9} mbar. Control experiments under identical sputtering conditions were conducted on Si wafer to determine if the TOF-SIMS analysis of the N-/S-LFP can be considered surface specific. Over the course of three hours of dynamic mode operation, less than 3 nm of material was sputtered, as determined by ex-situ atomic force microscopy measurements (data not shown). While differences in ionization efficiencies between Si and $LiFePO_4$ are unknown, the 1000 s of dynamic mode sputtering presented in Figure 1 represents interrogation of only first few monolayers of the material.

For the electrochemical analysis, 2032-type coin half-cells employing a Li-metal counter electrode and 1 M $LiPF_6$ in ED/DEC (1/1 in volume) liquid electrolyte were prepared. The composition of the cathode composite is $LiFePO_4$/Carbon/PTFE = 80:17:3 by weight. Rate capability and charge/discharge cycle performance were characterized with a LAND battery cycler (CT-2001A). For the rate capability measurement, the coin half-cells were charged to 4.5 V at the rate of C/10 in the constant-current mode and discharged to 2.5 V at various current densities from C/10 to 10C. For the cycle performance characterization, 1C charge/5C discharge for the initial 50 cycles and 5C charge/1C discharge for the next 50 cycles in the 2.5−4.5 V range were used as a standard condition to compare asymmetric charge/discharge cycle performance. A potential step chronocoulometry test was done with an Arbin BT-2000 system. After the galvanostatic charging to 4.5 V, the voltage was forced to jump down to each different value (3.4, 3.3, 3.2, 3.1, and 3.0 V) for an hour, and the capacity-transient data were recorded.

COMPUTATIONAL METHOD

All the calculations were performed in the Vienna ab initio simulation package (VASP) at the GGA+U level of theory.[20,21] The functional for electron exchange and correlation was chosen as PW91, and the effective U value, $U_{eff} = U − J$, was set to 4.3 eV, according to a self-consistent calculation.[18,22,23] Core electrons were described in the projected augmented wave formalism.[24] Valence electrons were described by a plane wave basis set with an energy cutoff at 400 eV.[25,26] A ferromagnetic spin configuration was set for the Fe ions. The supercell was constructed of 1 × 2 unit cells on the ac plane, and 8 layers in the b-direction, with 15 Å vacuum separating the periodic slabs.

ASSOCIATED CONTENT

Ⓢ Supporting Information

Additional figures as described in the text. This material is available free of charge via the Internet at http://pubs.acs.org.

AUTHOR INFORMATION

Corresponding Author
*E-mail: jgoodenough@mail.utexas.edu.

Notes

The authors declare no competing financial interest.

■ DEDICATION

His co-authors would like to congratulate Prof. John B. Goodenough on the occasion of his 90th birthday.

■ REFERENCES

(1) Padhi, A. K.; Nanjundaswamy, K. S.; Goodenough, J. B. *J. Electrochem. Soc.* **1997**, *144*, 1188.

(2) Yuan, L.-X.; Wang, Z.-H.; Zhang, W.-X.; Hu, X.-L.; Chen, J.-T.; Huang, Y.-H.; Goodenough, J. B. *Energy Environ. Sci.* **2011**, *4*, 269.

(3) Yamada, A.; Chung, S.; Hinokuma, K. *J. Electrochem. Soc.* **2001**, *148*, A224.

(4) Ong, S. P.; Jain, A.; Hautier, G.; Kang, B.; Ceder, G. *Electrochem. Commun.* **2010**, *12* (3), 427.

(5) Ravet, N.; Goodenough, J. B.; Besner, S.; Simoneau, M.; Hovington, P.; Armand, M. Abstract no. 127. *196th Meeting of the Electrochemical Society*, 1999.

(6) Ravet, N.; Chouinard, Y.; Magnan, J. F.; Besner, S.; Gauthier, M.; Armand, M. *J. Power Sources* **2001**, *97–98*, 503.

(7) Huang, H.; Yin, S.-C.; Nazar, L. F. *Electrochem. Solid State Lett* **2001**, *4* (10), A170.

(8) Nishimura, S.-I.; Kobayashi, G.; Ohoyama, K.; Kanno, R.; Yashima, M.; Yamada, A. *Nat. Mater.* **2008**, *7*, 707.

(9) Morgan, D.; der Ven, A. V.; Ceder, G. *Electrochem. Solid State Lett.* **2004**, *7*, A30.

(10) Islam, M.; Driscoll, D.; Fisher, C.; Slater, P. *Chem. Mater.* **2005**, *17*, 5085.

(11) Whittingham, M. S. *Chem. Rev.* **2004**, *104*, 4271.

(12) Trudeau, M. L.; Laul, D.; Veillette, R.; Serventi, A. M.; Mauger, A.; Julien, C. M.; Zaghib, K. *J. Power Sources* **2011**, *196*, 7383.

(13) Bai, Y.; Yin, Y.; Yang, J.; Qing, C.; Zhang, W. *J. Raman Spectrosc.* **2011**, *42*, 831.

(14) Susac, D.; Zhu, L.; Teo, M.; Sode, A.; Wong, K. C.; Wong, P. C.; Parsons, R. R.; Bizzotto, D.; Mitchell, K. A. R.; Campbell, S. A. *J. Phys. Chem. C* **2007**, *111*, 18715.

(15) Ellis, B.; Subramanya Herle, P.; Rho, Y.-H.; Nazar, L. F.; Dunlap, R.; Perry, L. K.; Ryan, D. H. *Faraday Discuss.* **2007**, *134*, 119.

(16) Dathar, G. K. P.; Sheppard, D.; Stevenson, K. J.; Henkelman, G. *Chem. Mater.* **2011**, *23* (17), 4032.

(17) Wang, L.; Zhou, F.; Meng, Y. S.; Ceder, G. *Phys. Rev. B* **2007**, *76*, 165435.

(18) Maxisch, T.; Zhou, F.; Ceder, G. *Phys. Rev. B* **2006**, *73*, 104301.

(19) Montella, C. *J. Electroanal. Chem.* **2002**, *518*, 61.

(20) Kohn, W.; Sham, L. J. *Phys. Rev.* **1965**, *140*, A1133.

(21) Kohn, W.; Becke, A. D.; Parr, R. G. *J. Phys. Chem.* **1996**, *100*, 12974.

(22) Perdew, J. P. In *Electronic Structure of Solids*; Ziesche, P., Eschrig, H., Eds.; Akademie Verlag: Berlin, 1991; pp 11–20.

(23) Zhou, F.; Cococcioni, M.; Marianetti, C. A.; Morgan, D.; Ceder, G. *Phys. Rev. B* **2004**, *70*, 235121.

(24) Kresse, G.; Joubert, D. *Phys. Rev. B* **1999**, *59*, 1758.

(25) Kresse, G.; Furthmuller, J. *Comput. Mater. Sci.* **1996**, *6*, 15.

(26) Kresse, G.; Furthmuller, J. *Phys. Rev. B* **1996**, *54*, 11169.

3218

dx.doi.org/10.1021/cm301569m | *Chem. Mater.* 2012, 24, 3212–3218